Supporting information

Unreacted PbI_2 as a Double-Edged Sword for Enhancing the Performance of Perovskite Solar Cells

T. Jesper Jacobsson[1,2], Juan-Pablo Correa-Baena[2], Elham Halvani Anaraki[2,3], Bertrand Philippe[4], Samuel D. Stranks[5,6], Marine E. F. Bouduban[7], Wolfgang Tress[8], Kurt Schenk[9], Joël Teuscher[7], Jacques-E. Moser[7], Håkan Rensmo[4], Anders Hagfeldt[2,10]

1) University of Cambridge, Department of Chemistry, Lensfield Road, Cambridge CB2 1EW, UK
2) Laboratory for Photomolecular Science, Institute of Chemical Sciences and Engineering, École Polytechnique Fédérale de Lausanne, CH-1015-Lausanne, Switzerland
3) Department of Materials Engineering, Isfahan university of Technology, Isfahan, 84156-83111, Iran
4) Department of Physics and Astronomy, Uppsala University, Box 516, 75120, Uppsala, Sweden
5) Research Laboratory of Electronics, Massachusetts Institute of Technology, 77 Massachusetts Avenue, Cambridge, Massachusetts 02139, United States
6) Cavendish Laboratory, JJ Thomson Avenue, Cambridge CB3 0HE, United Kingdom
7) Photochemical Dynamics Group, Institute of Chemical Sciences and Engineering, École Polytechnique Fédérale de Lausanne, CH-1015-Lausanne, Switzerland
8) Laboratory of Photonics and Interfaces, Institute of Chemical Sciences and Engineering, École Polytechnique Fédérale de Lausanne, CH-1015-Lausanne, Switzerland
9) École Polytechnique Fédérale de Lausanne, CH-1015-Lausanne, Switzerland
10) Department of Chemistry - Ångström Laboratory, Uppsala University, Box 538, 75121 Uppsala, Sweden

Jacobsson.jesper.work@gmail.com , +46 (0)70-5745116
Anders.hagfeldt@epfl.ch, +41 (0)21 693 53 08

Experimental Methods

Perovskite and device preparation

As substrate for the devices, FTO NSG 10 was used. The substrates were cleaned in freshly prepared piranha solution composed of five parts concentrated H_2SO_4 and two parts 30 % H_2O_2. Proper protection should be used while handling this solution as it is highly aggressive. The substrates were soaked in the piranha solution for 10 minutes and then rinsed in water and then ethanol. They were thereafter treated in a UV-ozone cleaner for 10 minutes.

A hole blocking layer of TiO_2 was deposited on the cleaned FTO substrates using spray pyrolysis. The spray solution was composed of ethanol, acetyl acetone, and titanium diisopropoxide (30% in isopropanol) in the proportions 90:4:6 by volume. Oxygen at a base pressure of 1 bar was used as a carrier gas. The glass substrates were heated to 450°C on a hotplate and kept at that temperature for 15 minutes prior to the spraying. After an additional 30 minutes at 450°C, the sprayed glass substrates were slowly cooled to room temperature. 10 ml of spray solution was used to cover 40 cm^2 of substrates. This procedure gives a compact layer of anatase with a thickness of around 20-30 nm.

On top of the compact TiO_2-layer deposited by spray pyrolysis, a mesoporous scaffold of TiO_2 nanoparticles was deposited by spin-coating. TiO_2 paste (30 NR-D) was bought from Dyesol and was dissolved in ethanol at a concentration of 150 mg/mL. On each substrate (1.4·2.4 cm) 50 µL of the TiO_2 solution was applied and spin-coated at 4000 rpm, with an acceleration of 2000 rpm/s, for 10 s. A piece of scotch tape was used on one side of the substrates to prevent the mesoporous TiO_2 to form where the front contacts were to be deposit. The substrates with mesoporous TiO_2 were sintered at 450ºC in air on a hot plate for 30 minutes and then slowly cooled to ambient temperature.

For XRD-measurements, and time dependent spectroscopy, the perovskites were deposited on soda lime glass (SLG) covered by 15 nm amorphous SnO_2. The SnO_2 film increases the wettability of the precursor solutions that give perovskite films of higher quality. The SnO_2 was deposited by atomic layer deposition, ALD, at 120°C using a Savanah ALD 100 from Cambridge Nanotech Inc. As a tin precursor, Tetrakis(dimethylamino)tin(IV), bought from Stem Chemicals Inc., was used. Ozone was used as the oxidising agent. The ozone was produced by an ozone generator fed with oxygen gas (99.9995% pure, Carbagas) producing O_3 at a concentration of 13% in O_2. Nitrogen was used as a carrier gas with a flow rate of 5 sccm. The substrates with SnO_2 were directly prior to perovskite deposition treated in a UV-ozone cleaner for 10 minute. This process for deposition of an electron selective SnO_2 contact is described in more detail in a previous publication[1], and has been used as an electron selective contact in high efficiency planar devices[1].

For PL-mapping measurements, the perovskites were deposited on thin microscope cover glass slides. For those measurements the perovskite was deposited on: glass, glass/TiO_2, glass/Al_2O_3, glass/TiO_2/mesoporous TiO_2, glass/TiO_2/mesoporous TiO_2/Al_2O_3. The Al_2O_3 was deposited by ALD and was a few nm thick.

Prior to perovskite deposition, the substrates with mesoporous TiO_2 underwent a lithium treatment which has been found to be beneficial for the device performance[2]. On the substrates, 100 µL of a 35mM Lithium bistrifluoromethanesulfonimidate (Li-TFSI) in acetonitrile was applied and spun at 3000 rpm for 10 s. The substrates were then thermally annealed in air at 450°C for 30 minutes and then slowly cooled to 150ºC where after they were brought directly into a glovebox for perovskites deposition.

The best perovskite cells presented in the literature are based on mixed lead perovskites using a mixture of bromide and iodide on the halogen position and a mixture of methyl ammonium and formamidinium as organic ion. The best perovskites have a composition around $MA_{2/6}FA_{4/6}Pb(Br_{1/6}I_{5/6})_3$[3].

In previous work, we have observed that a slight molar excess of PbI_2 with respect to ([MA] + [FA]) in the precursor solutions from which the perovskite is deposited have been beneficial for device performance[4,5]. In a previous work, the [Pb^{2+}] / ([MA] + [FA]) ratio for all precursor solutions was held at 1.1[3]. As the effect we intend to probe in these experiments is the importance of PbI_2, the FAI-concentration in the precursor solution was varied but [MABr] was held constant and equal to [$PbBr_2$]. This is a step away from the optimized protocol but makes the parameter window slightly cleaner for this particular investigation.

The solutions were prepared in a glovebox with nitrogen atmosphere. Stock solutions of PbI_2 and $PbBr_2$ were prepared in advance whereas the final precursor solutions were prepared just before perovskite deposition. The solvent used for the perovskite solutions was a mixture of anhydrous dimethyl formamide, DMF, and anhydrous dimethyl sulfoxide, DMSO in the proportion 4:1 by volume. Three master solutions were prepared; PbI_2 and CH_3NH_3I in DMF/DMSO with a stoichiometric excess of PbI_2, PbI_2 and CH_3NH_3I in DMF/DMSO with a stoichiometric deficiency of PbI_2, and $PbBr_2$ and $CH(NH_2)_2Br$ in DMF/DMSO. These three solutions were mixed in the right proportions to get the final precursor solutions from which the perovskites were deposited.

All the final precursor solutions had the following concentrations: [Pb2+] = 1.25 M, [$PbBr_2$] = 0.22 M, [PbI_2] = 1.04 M, [MABr] = [$PbBr_2$] = 0.22 M. The concentration that was varied in the precursor solutions was [FAI]. When we henceforth state that a composition is +10 % with respect to PbI_2, we mean that [FAI] = [PbI_2]·0.9, and when we state a composition as -10 % we mean that [FAI] = [PbI_2]·1.1. Plus 10% thus mean a surplus of PbI_2 in the solution (or a deficiency of FA), and that should result in some excess PbI_2 in the films. There could in principle be $PbBr_2$ in the film as well, but as $PbBr_2$ more easily form the perovskite than PbI_2 that is unlikely[3]. A secondary effect of this procedure is that the film thickness may vary a bit as a function of stoichiometry, but that should not be a mayor effect and can be compensated for.

The MA and FA salts were bought from Dyesol and the lead salts were bought from TCI. All chemicals were used as received without further treatment. The perovskites were spin-coated in a glove box with a flowing nitrogen atmosphere with a fairly high flow in order to ventilate out solvent vapors. For each sample, 35 μL of the precursor solution was spread over the substrate, which thereafter was spin-coated using a two-step program. The first step was a spreading step using a rotation speed of 1000 with an acceleration of 200 rpm/s rpm for 10 s. That step was immediately, without pause, followed by the second step where the films were spun at 4000 rpm for 30 s using an acceleration of 2000 rmp/s. During the second step, when approximately 15 seconds of the program remains, 100 μL of anhydrous chlorobenzene was applied on the spinning film with a hand held automatic pipette. This last step, known as the antisolvent method, has a large impact on film morphology and result in significantly better device performance[6-8]. It is, however, one of the steps that introduce a palpable degree of artisanship into the process.

Directly after spin-coating, the films were placed on a hotplate at 100°C where they were annealed for 30-70 min. At this temperature, the transformation into the perovskite was visually seen to occur within the time frame of a minute.

After the heat treatment, the samples were cooled to ambient temperature where after the solid state hole-conductor was spin-coated on top of the films. A 70 mM solution of Spiro-MeOTAD (spiro) dissolved in chlorobenzene was used as a hole conductor. To improve the performance of the spiro, three different additives were added[9,10]: 4-*tert*-butylpyridine, 1.8 M Li-TFSI in acetonitrile, and 0.25 M Co[t-BuPyPz]$_3$[TFSI]$_3$, also known as FK209, in acetonitrile. The Spiro:FK209:Li-TFSI:TBP molar ratio was 1:0.05:0.5:3.3. The spiro solution was prepared the same day as the perovskite films were deposited.

The spiro was deposited by spin-coating at 4000 rpm for 20 s. 50 μL of the solution was deposited on the spinning film, using a hand held automatic pipet, a few seconds into the

spinning program. The samples were stored in a desiccator pumped under vacuum for a day and the back contact was then deposited.

Before the back contact was deposited, the perovskite/spiro layer was removed from one end of the samples using a razorblade, acetonitrile, and a cotton bud in order to ensure contact between the FTO and the gold contact. The front and back contact were composed of an 80 nm thick gold film deposited by physical vapor deposition at a pressure of around $2 \cdot 10^{-5}$ Torr using an evaporator from Leica, EM MED020.

Characterization

UV-vis absorption measurements were performed on an Ocean Optics spectrophotometer HR-2000 c with deuterium and halogen lamps. In all measurements, a full spectrum from 190 to 1100 nm with 2048 evenly distributed points was sampled. 100 consecutive spectra were averaged in order to obtain good statistics.

Steady state photoluminescence was measured with a Fluorolog, Horiba Jobon Yvon, FL-1065. A white tungsten lamp was used as luminous source, A monochromator was placed between the sample and the light source as well as between the sample and the detector. An excitation wavelength of 435 nm was used for all samples. The excitation spectrum was measured from 455 nm to 835 nm in steps of one nm. An integration time of 0.5 s was used for each wavelength. Measurements were performed both on perovskites deposited on substrates with mesoporous TiO_2 and on films deposited on substrates with 15 nm amorphous SnO_2. The excitation source and the detector were placed in 90º with respect to each other. The sample was oriented 60° with respect to the excitation source in order to decrease interference form reflected light.

XRD measurements were measured using a Brucker diffractometer using a Bragg-Brentano geometry. $Cu_{k\alpha}$ radiation, with a wavelength of 1.54 Å, form a cupper target was used as X-ray source. 2θ scans between 10° and 65º were collected using a step size of 0.008º.

SEM imaging was carried out using a Zeiss Merlin scanning electron microscope. Photographs were taken using a Canon EOS 450 D with an EFS 60 macro lens.

The IV-characteristics of the devices were measured using a home built system. To simulate solar light, an Oriel solar simulator with a xenon arc lamp, fed with 450 W input power, was used together with a Schott K113 Tempax filter (Praäzisions Glas & Optik GmbH). The light intensity was calibrated with a silicon photodiode equipped with an IR-cutoff filter (KG3, Schott). The IV-curves were measured with a digital source meter (Keithley 2400). No equilibration time or light soaking was applied before the potential scan. The starting point for the measurements was chosen as the voltage where the cell provided approximately 2 mA in forward bias. From that point, the potential was scanned to short circuit and back again using a scan speed of 20 mV/s. Thereafter, the dark current was sampled using the same scan speed. The cells were masked with a metal mask in order to limit the active cell area to 0.16 cm^2. The scan speed was slow enough to give efficiency data for the backwards scan that are in reasonable agreement with maximum power point tracking measurements. IV-curves measured on high efficiency devices with this setup have recently been confirmed to be in good agreement with data provided from independent certification agencies.

The external photocurrent efficiency, *EQE*, was measured on a subset of the samples. This was done by a home built system composed of a 300 W xenon lamp, a gemini-180 double monochromator and a lock in amplifier. A white bias light of 50 W/m^2 was provided by a LED array. The *EQE* for each wavelength was extracted by measuring the difference in short circuit current between the white bias light, and the white bias light together with a superimposed monochromatic light, and scaling the signal with the intensity of the monochromatic light. The monochromatic light was chopped at 2 Hz and to get reasonable statistics, a fairly long integration time was used. The *EQE* was measured in steps of 10 nm from 340 to 850 nm. The EQE- system has had some performance problems. Absorption onsets and relative intensities are trustworthy but too much significance should not be read into absolute values.

Transient absorbance spectra were recorded using femtosecond pump-probe spectroscopy. The pump beam (λ_{ex} = 480 nm, 46 fs FWHM) was obtained by pumping a two-stage Non-collinear Optical Parametric Amplifier (NOPA) with the output of a Ti:Sapphire laser (CPA-2001, Clark, 778 nm, 120 fs, 1KHz repetition rate). The pump fluence at the sample was 35 μJcm^{-2} (100 nJ, 605 μm in diameter). The probe pulse was generated by directing a part of the 778 nm-output into a CAF_2 crystal, yielding a white light continuum (WLC, 400 nm-780 nm). The probe fluence at the sample was much lower than the one of the pump. Similarly, its diameter was smaller than the one of the pump to ensure homogeneity of the probed area. The dynamics of the photoinduced signals were obtained with a computer-controlled delay-line on the pump path. The probe beam was split before the sample into a beam going through the sample (signal beam) and a reference beam. Both signal and reference pulses were directed to a pair of 163 mm spectrographs (Andor Technology, SR163) and detected pulse-to-pulse with 512x58 pixels back-thinned CCD detectors (Hamamatsu S07030-0906). The pump beam was chopped at half the laser frequency (500Hz). Satisfying signal-to-noise ratio was obtained by averaging 3000 spectra.

TEM images were taken by a Talos FEI microscope. Samples were prepared with two different compositions (-10 % and + 20 %). Those samples were deposited directly on soda lime glass. The perovskite film was scraped of using a razor blade and deposited on the TEM grid by rubbing it in the perovskite scrapes.

Photoelectron spectroscopy measurements were performed at two different synchrotron facilities having two different energy ranges. The depth sensitivity in the PES measurements depends on the inelastic mean free path (IMFP) of the photoelectrons, which is related to their kinetic energy. Therefore, changing the photon energy will modify the depth sensitivity[11]. The depth sensitivity values reported in the present work were defined as three times the IMFP of the photoelectron, since 95% of the PES signal in a homogeneous material comes from a layer with this thickness.

Hard X-ray PES (HAXPES) was carried out at BESSY II (Helmholtz Zentrum Berlin, Germany) at the KMC-1 beamline[12] using the HIKE end-station[12]. The end-station is provided with a usable photon energy range from 2 keV to 12 keV, the photon energy is selected using a double-crystal monochromator (Oxford-Danfysik) and the photoelectron kinetic energies (KE) were measured using a Model R4000 analyzer (Scienta) optimized for high kinetic energies. In this work, photon energies of 2100 eV and 4000 eV were used by selecting the first-order light from a Si(111) and Si(311) crystals, respectively. The pressure in the analysis chamber was ~ 10^{-8} mbar.

Soft X-ray Photoelectron spectroscopy (SOXPES) measurements were carried out at the Beamline I- 411 at the Swedish National Synchrotron Facility MaxIV Laboratory in Lund, Sweden[13]. The end-station is in this case provided with a usable photon energy range from 50 eV to 1500 eV. The photon energies were selected using a modified Zeiss SX-700 monochromator, and the photoelectron kinetic energies (K.E.) were measured using a Scienta R4000 WAL analyzer. The pressure in the analysis chamber was ~10^{-8} mbar.

Overview spectra were measured with a pass energy (Ep) of 500 eV while 200 eV was used for core peaks and valence band spectra. The spectra presented in this work were energy calibrated versus the Fermi level at zero binding energy, which was determined by measuring a gold plate in electric contact with the sample and setting the Au $4f_{7/2}$ core level peak to 84.0 eV after curve fitting. The perovskite related spectra were intensity calibrated vs. the $Pb4f_{7/2}$ core level peak if not stated otherwise. The peak positions and areas were optimized by a weighted least-squares fitting method using CasaXPS software. Finally, the quantification tables and intensity ratios presented between different core levels were calculated from the experimental results after correcting the intensity by the photoionization cross section for each element at their specific photon energy, using database values[14,15].

Charging was controlled by following peak positions and peak shape with variations in light intensity and time. No charging was observed in the measurements of the different perovskite

materials. The same procedure was also used to check for X-ray-induced effects. No changes were observed in the spectra reported here.

After preparation of the perovskite materials, each sample was stored in a sealed box together with common desiccants to avoid any moisture contamination. The box was only opened prior the PES analysis.

Confocal photoluminescence (PL) maps were acquired using a custom-built time-correlated single photon counting (TCSPC) confocal microscope (Nikon Eclipse Ti-E) setup with a 100X oil objective (Nikon CFI PlanApo Lambda, 1.45 NA). Samples were photoexcited through the glass-side using a 405 nm laser head (LDH-P-C-405, PicoQuant GmbH) with pulse duration of <90 ps, fluence of ~2 $\mu J/cm^2$/pulse, and a repetition rate of 0.5 MHz. The photoluminescence from the sample was collected by the same objective and the resulting collimated beam passes through a long-pass filter with a cut-off at 416 nm (Semrock Inc., BLP01-405R-25) to remove any residual scattered or reflected excitation light. A single photon detecting avalanche photodiode (APD) (MPD PDM Series 50 mm) is used for the detection, with the APD output connected to a timing module with a resolution of 4 ps (PicoQuant PicoHarp 300), which detects the arrival time of each photon for the TCSPC measurements. The sample was scanned using a piezoelectric scanning stage. The measurements were acquired using the commercial software SymphoTime 64 (PicoQuant GmbH). For the measurements when exciting and detecting through the top-side, a 40X objective (Nikon PlanApo, 0.95 NA) was used.

Electroluminescence measurements were performed using a Biologic SP300 Potentiostat as voltage source and current meter. The emitted photon flux was detected by measuring the short-circuit current of a Hamamatsu photodiode (1 cm^2), connected to a second channel of the potentiostat while sweeping the voltage applied to the solar cell.

Additional XRD data

As discussed in the main article, XRD data was sampled for films of seven different stoichiometries. The full set of diffractograms are given in figure S.1.

Apart from the perovskite phase, the only crystalline phase observed is PbI_2, which, as expected, increases in amount for the more over-stoichiometric samples. PbI_2 is detected also in the under-stoichiometric samples but in a much smaller amount. Crystalline $PbBr_2$ is not detected in any sample, which is in line with previous measurements where $PbBr_2$ was shown to have a stronger preference for forming the perovskite than PbI_2[3]

Depending on the composition, the perovskite crystal phase can be either tetragonal or cubic at room temperature. The crystalline phase here observed is cubic for all samples, which most easily is seen as the absence of a diffraction peak at 23.5° and that the (022) peak around 40.5° is a single peak rather than the double peak expected for the tetragonal phase. Based on previous measurements[3,16] as well as on theoretical considerations[17], that is the expected result.

The width of the diffraction peak which is wider for the under-stoichiometric samples. That indicates a smaller crystallite size. No clear trend is, however, observed. The under-stoichiometric samples have one wider peak, whereas the rest of the samples have one narrower peak. An estimation based on Scherrer's equation gives a crystallite size of around 30 nm for the under-stoichiometric samples. For the over-stoichiometric samples, the same approach gives more than 100 nm but for crystallite this large it is hard to get a good estimate, and due to the instrument broadening this is bound to be an underestimation

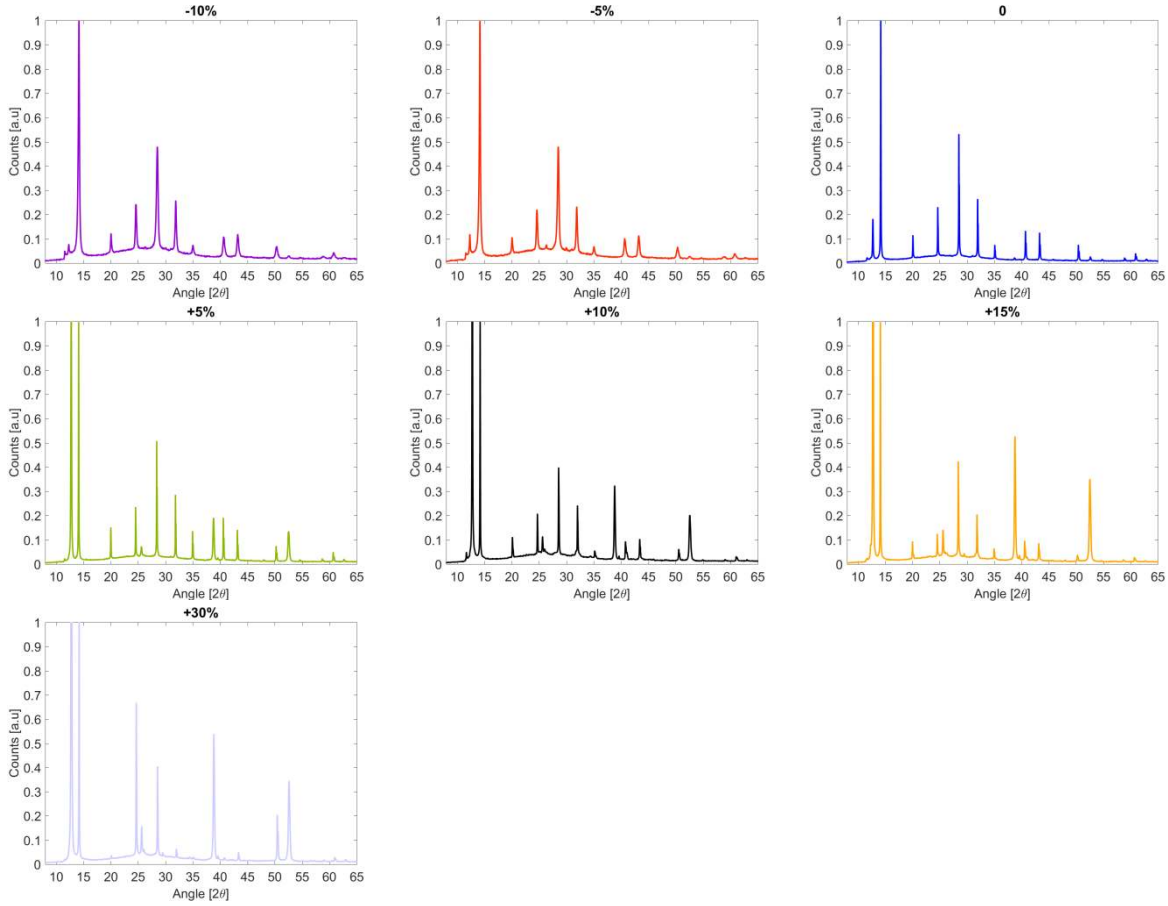

Figure S.1. XRD data for a number of different stoichiometry. Starting from the upper left corner and going from left to right the compositions are: -10 %, -5 %, 0 %, 5 %, 10 %, 15 %, 30% according the notation established in the experimental section. Data is normalised with respect to the (100) reflection around 14.2ºC.

Additional absorption data

Absorption data measured in transmission mode for seven different stoichiometries were given in the main article. These data are here reproduced in figure S.2.a. The overall absorption behaviour was rather unaffected by the stoichiometry, with the exception of the most under-stoichiometric sample (the one with the greatest deficiency of the PbI_2). That sample has a more plateau-like absorption in a region just above the band gap. The background signal due to scattering is low, and below 0.1 for all samples which is a sign of uniform films of high quality with respect to macroscopic inhomogeneity. The value of the background, hear simply defined as the minimum absorption value, was removed in the subsequent data treatment and are given in figure S.2.c.

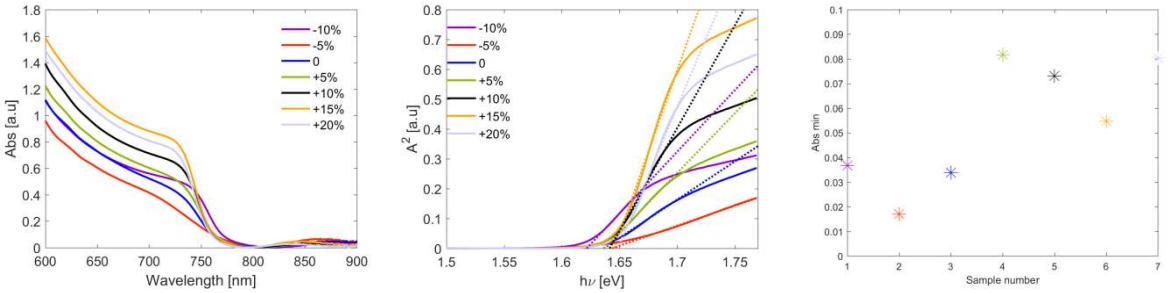

Figure S.2. (a) Absorption as a function of wavelength. Data are background corrected. (b) Square of the absorption against photon energy for extracting band gap energies. (c) The background signal due to scattering that is subtracted from the raw data to give the absorption curves in (a) The colour scheme is the same as in (a) and (b).

The absorption data in figure S.2.a indicates that films with an excess of PbI_2 absorb stronger than the films with less PbI_2. Cross section SEM images presented in figure S.4 indicate that the films are of essentially the same thickness, and complementary measurements using an integrating sphere indicate that it may be differences in reflectivity that are behind the apparent absorption difference in figure S.2.a. That could potentially be an effect of difference in surface roughness observed in the SEM images in figure S.4 and S.5. Absorption measurements measured in reflection mode using an integrating sphere was measured for a few samples as illustrated in figure S.3. Those data indicate that the transmission measurements were overestimating the difference in absorption strength, and that the absorption coefficient not are strongly affected by the stoichiometry.

A lower overall absorption, be it due to lower absorption itself or higher reflectivity, may correlate with a lower photocurrent for the under-stoichiometric samples as discussed in the main article.

The rise in absorption for the -5% sample is less steep than for the other samples. That could possibly relate to the increased FWHM seen for the 001 diffraction peak (figure 2.b). The -10 % sample which has the same FWHM does, however, not show the same absorption behaviour.

In figure S.2.b, the square of the absorption is plotted against photon energy. By doing that, a linear region is found for photon energies slightly above the band gap energy. If that linear region is extrapolated, the band gap is given as the intercept with the base line. The extracted band gap values are given in table S.1. They are centered around 1.64 eV. There is a tendency for the band gap to increase for the samples with more PbI_2 but the effect is small; 1.62-1.65eV and less than 0.01 eV if the sample with the smallest amount of PbI_2 is excluded. As the band gap is strongly dependent of the Br/I ratio this could indicate a slight compositional change. The effect is too small to be of real significance and both the absorption measurements and the XRD-data indicate that the crystalline perovskite phase is not strongly affected by the amount of PbI_2 in the system, even though the crystal grain size may differ.

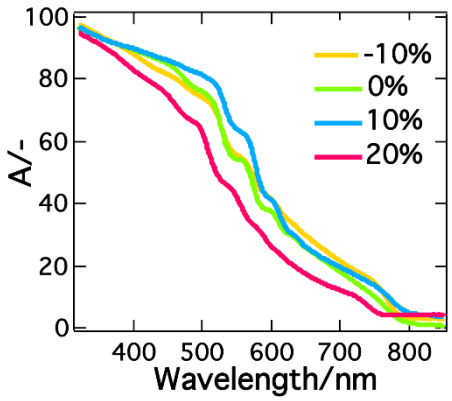

Figure S.3. Absorbance as a function of wavelength for samples of four different stoichiometries. The measurements were performed in reflection mode using an integrating sphere.

Table S.1. Extracted band gap as a function of composition

Sample number	Stock	E_g [eV]
1	-10%	1.62
2	-5%	1.64
3	0	1.64
4	5%	1.64
5	10%	1.64
6	15%	1.65
7	20%	1.65

Additional SEM data

Cross section SEM-images of complete cells are displayed in figure S.4, which show that the film thickness is rather unaffected by the stoichiometry. The over-stoichiometric samples may be slightly thinner, which would be expected as the amount of perovskite that could form from a given volume of stock solution is somewhat smaller for the over-stoichiometric samples given the synthesis protocol used. The difference is, however, small.

Top view SEM images of a sample with -10% and + 20% stoichiometry was given in the main article. In figure S.5, the corresponding figures for a broader range of stoichiometries are given. Larger version, and images of different magnification are given in the end of the supporting information.

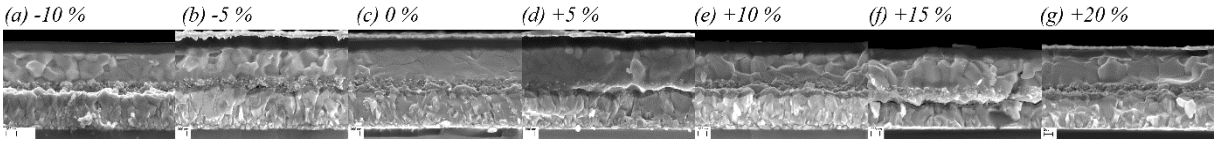

Figure S.4. Cross section SEM images of cells with seven different stoichiometry. The most under-stoichiometric sample is the left one (a) and the most over-stoichiometric samples with most PbI_2 is to the right (g). Depending of the quality of the edge of the brake the individual grains are more or less clearly seen. The top most gold contact is only seen in (b), (c), (d) and (g), and in (a), (e) and (f) the best view was found slightly outside the gold contact region. The scale bare is 200 nm.

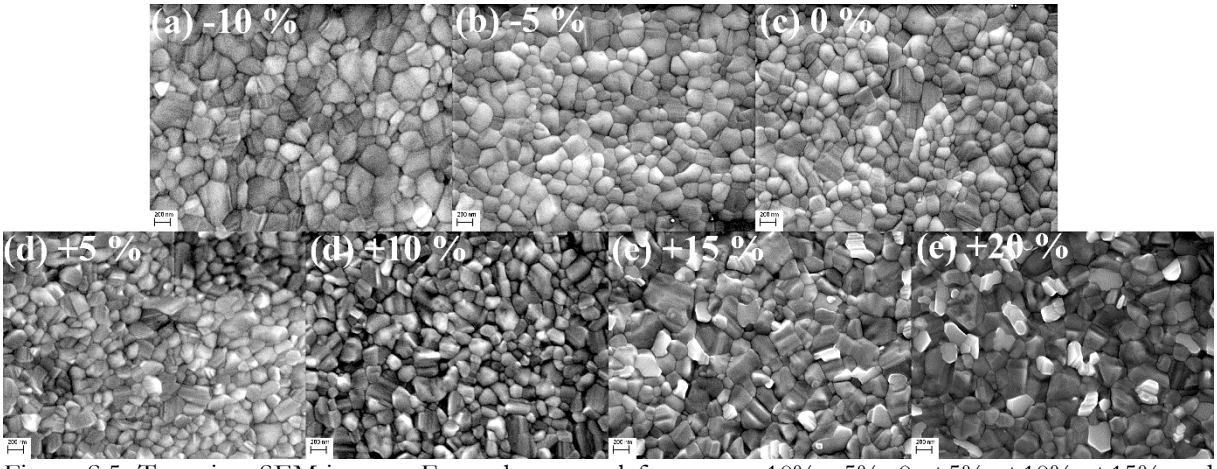

Figure S.5. Top view SEM-images. From the upper left corner: -10%, -5%, 0, +5%, +10%, +15% and +20%. The scale bars are 200 nm.

Additional photoluminescence data

An interesting observation is that the PL-intensity is distinctly higher for the sample with a deficiency of PbI_2. The higher PL-intensity for the samples with less PbI_2 is a solid observation, but the magnitude of the difference is uncertain as the setup does not give absolute numbers which also have been observed to vary depending on sample and time. This effect was seen for most batches but not for every single one which is an indication that competing mechanisms are involved in determining the emissivity of the samples and that it to some extent is batch dependent.

On the day of synthesis, the difference in intensity was approximately one order of magnitude, as seen in figure S.6.a. After a month in dry air, this difference remains, but it gets somewhat smaller as seen in figure S.6.b. In figure S.6.a and S.6.b there appears to be a difference in absolute intensity, which could be the case, but as the setup used in the measurements not give absolute numbers that is not a solid conclusion. The corresponding normalised data is given in figure S.6.c-d. The peak positions are given in table S.2. No systematic shift is observed in the peak positions, neither with respect to storage time or stoichiometry. This indicates that the

perovskite composition is rather unaffected by the overall stoichiometry in the precursor solutions.

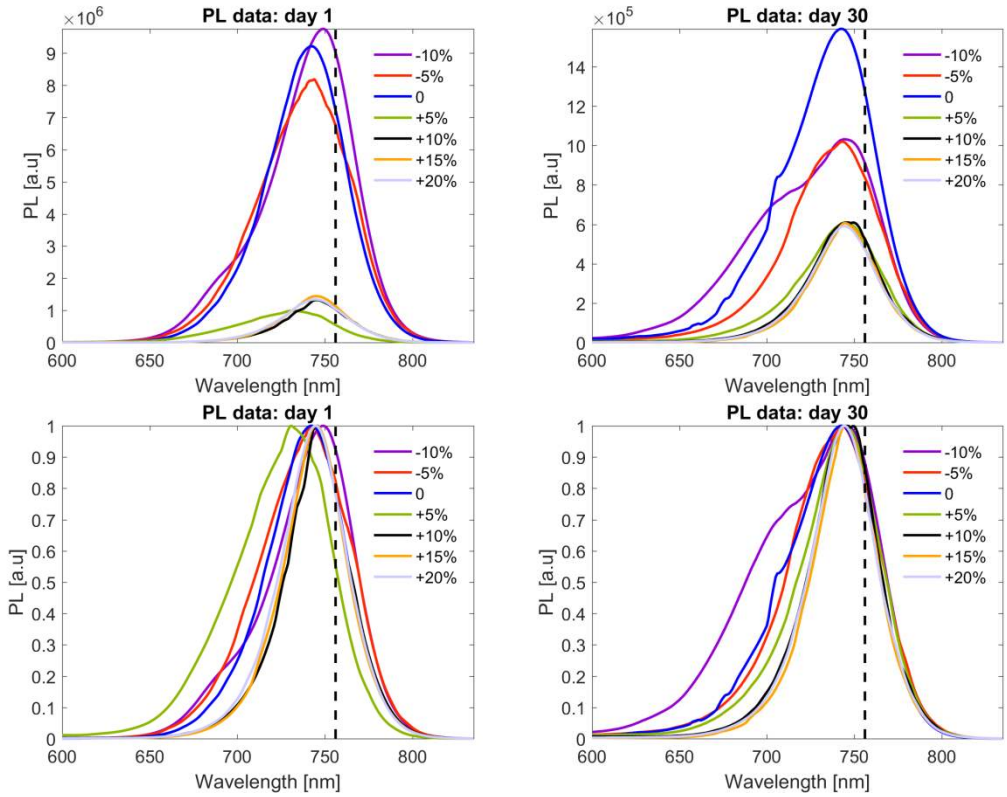

Figure S.6. (a) PL-data measured the same day as the films were deposited. (b) PL-data measured after one moth of storage in dry air. (c) Normalised data measured on day 1. (d) Normalised data measured after one moth of storage in dry air.

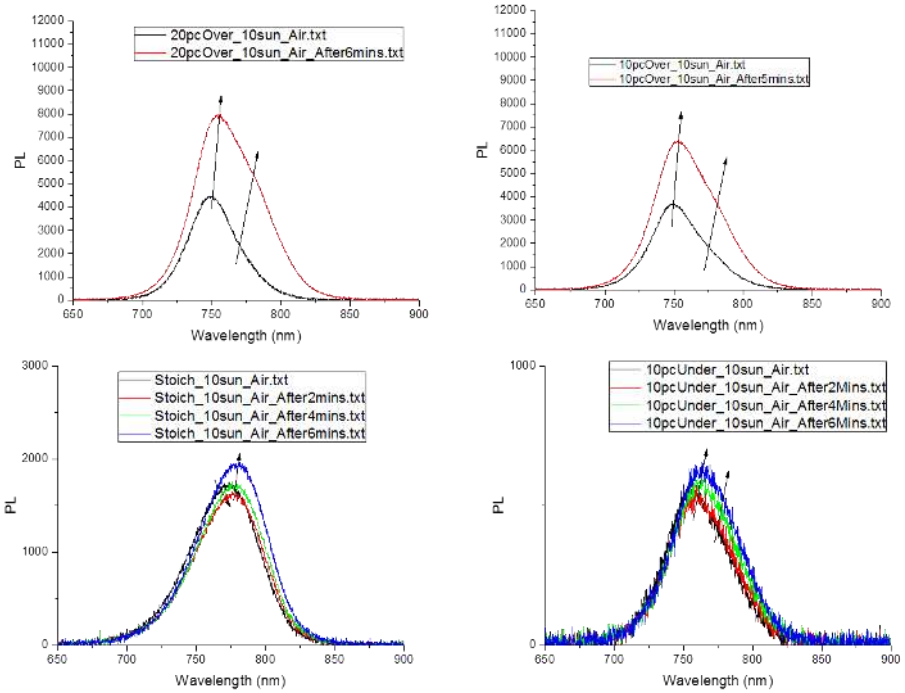

Figure S.7. PL data under 10 sun illumination, both directly while illuminated and after a few minutes of constant illumination.

In figure S.7 PL data were sampled both directly wile illuminated and after a few minutes of constant illumination (10 sun). For the over-stoichiometric samples there appears to be an increase in the intensity, and it also appears that a phase separation is occurring. For the stoichiometric sample and for the under-stoichiometric sample the effect is less evident.

Table S.2 Peak positions for the photoluminescence

Sample number	Stock	E_g [eV]	Peak position [nm] Day 1	Day 30
1	-10%	1.62	749	744
2	-5%	1.64	744	743
3	0	1.64	742	743
4	5%	1.64	731	745
5	10%	1.64	746	745
6	15%	1.65	745	745
7	20%	1.65	745	744

Additional photoelectron spectroscopy data

The C1s spectra are given in figure S.8. The measurement at 4000 eV gives similar conclusion whereas the measurement at 758eV mainly detected the surface contamination species mentioned earlier. In figure S.9 the relative percentage of Pb, I and Br in the mixed perovskite with three different stoichiometry as function of the photon energy.

The band gaps extracted earlier in this work were insensitive to the stoichiometry and the amount of excess PbI_2. This statement is confirmed by valence band spectra presented in figure 10. The spectra of the perovskite materials with composition -10%, 0 and +10% perfectly overlapped each other and a closer look at the valence band edge do not reveal any difference greater than the resolution of the technique which is ±0.05 eV.

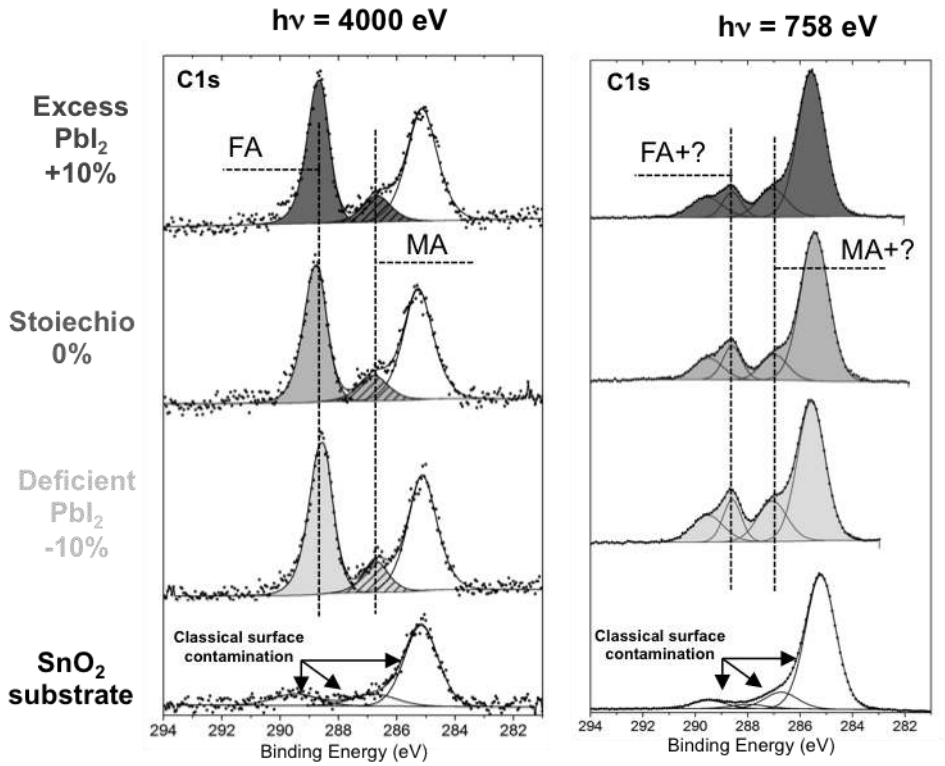

Figure S8: C1s core level peaks of the perovskite materials with three different stoiechiometries: -10%, 0, +10% in light grey, grey and dark grey respectively recorded at 4000 eV (left) and 758 eV (right). The C1s spectra of the SnO_2 substrate are shown as a reference to show the influence of the surface contamination on these spectra and how it mainly contributes to the signal when a low photon energy is used, i.e. a great surface sensitivity is probed.

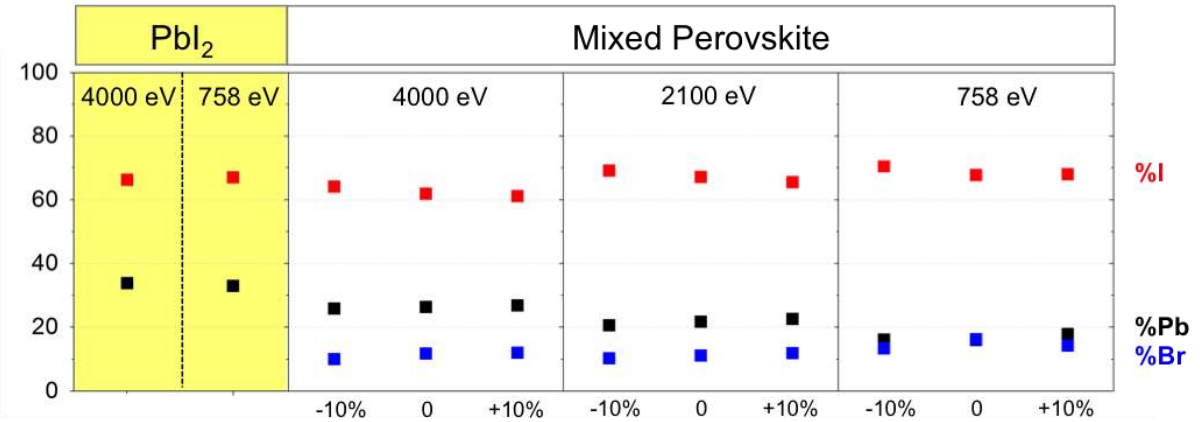

Figure S.9: Relative percentage of Pb, I and Br in the mixed perovskite with three different stoichiometry as function of the photon energy.

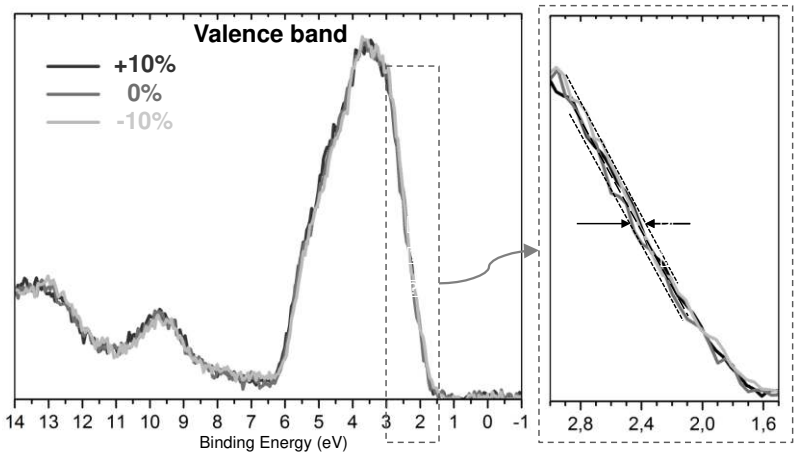

Figure S.10. Valence band spectra of the perovskite materials with three different stoichiometry: -10%, 0, +10% in light gray, gray and dark gray respectively recorded with a photon energy of 2100 eV. An expanded view of the valence band edge is presented on the right.

Additional device data

Making an efficient device is tricky, involves a fair bit of artisanship, and is affected by a number of environmental parameters that are challenging to control and at the moment not properly understood. This is the reason for the cell-to-cell and a batch-to-batch variation of device performance observed by many groups in the field, as well as in our data. The full set of JV-curves discussed in the article are given in figure S.11. The corresponding device data are given in table S.3

The absorption data in figure 2.c in the main article indicate that the under-stoichiometric samples have a lower absorbance which could explain a part of the drop in photocurrent. The magnitude of the current drop, together with the cross section SEM-images in figure S.4 and complementary absorption measurements using an integrating sphere, however, indicate that it cannot be ascribed to differences in film thickness and optical absorption.

If obstruction of ion motion is the reason behind the decrease in the hysteresis for the under-stoichiometric samples, grain size could be a contributing factor. As discussed above, the under-stoichiometric samples have more polycrystalline grains, or grains with more stacking defects, which could contribute to decreasing the ion movement, and thus also the hysteresis. A relation between smaller grains and a lower hysteresis does, however, not translate into over-stoichiometric compositions where the hysteresis has been observed to increase with decreased grain size[18].

Figure S.11. The full set of JV-curves

Table S.3. Device data extracted from the IV curves in figure S.1. An * marks data for the forward scan. The other data is for the reversed scan.

Stock [%]	Cell	V_{oc} [V]	J_{sc} [mA/cm²]	FF	η [%]	V_{oc}* [V]	J_{sc}* [mA/cm²]	FF*	η* [%]	H
-10	C1	1.20	12.8	0.64	10.0	1.20	12.8	0.56	8.6	0.06
-10	C2	1.20	14.4	0.66	11.4	1.19	14.4	0.55	9.4	0.08
-10	C3	1.20	17.6	0.66	13.9	1.19	17.6	0.68	14.3	-0.01
-10	C4	1.16	19.1	0.62	13.7	1.18	19.0	0.64	14.2	-0.02
-5	C1	1.18	15.4	0.62	11.3	1.19	15.4	0.61	11.0	0.01
-5	C2	1.11	15.9	0.61	10.9	1.13	16.0	0.58	10.6	0.01
0	C1	1.08	18.4	0.66	13.0	1.10	18.4	0.58	11.9	0.02
0	C2	1.12	18.2	0.62	12.8	1.14	18.2	0.59	12.4	0.01
0	C3	1.13	18.7	0.65	13.7	1.16	18.7	0.64	13.8	-0.02
0	C4	1.16	16.8	0.63	12.2	1.18	16.8	0.63	12.5	-0.02
+5	C1	1.14	21.6	0.69	17.1	1.17	21.6	0.65	16.3	0.01
+5	C2	1.12	21.1	0.67	15.9	1.15	21.1	0.65	15.6	0.00
+10	C1	1.07	22.0	0.67	15.9	1.07	22.0	0.57	13.2	0.07
+10	C2	1.06	21.7	0.62	14.3	1.05	21.8	0.57	12.9	0.05
+10	C3	1.15	22.2	0.68	17.4	1.15	22.1	0.70	17.9	-0.01
+10	C4	1.13	20.5	0.69	16.0	1.14	20.5	0.70	16.3	-0.01
+15	C1	1.03	21.6	0.68	15.2	1.02	21.5	0.55	12.0	0.10
+15	C2	0.99	21.7	0.53	11.0	0.97	21.6	0.43	9.1	0.14
+20	C1	1.09	21.7	0.72	17.4	1.09	21.7	0.52	12.2	0.12
+20	C2	1.12	21.6	0.73	17.7	1.13	21.7	0.58	14.2	0.08
+20	C3	1.13	19.6	0.72	15.9	1.12	19.6	0.63	13.9	0.04
+20	C4	1.12	22.7	0.71	18.1	1.12	22.7	0.60	15.4	0.05

Electroluminescence

Electroluminescence measurements were performed on the devices to verify whether the high open-circuit voltage correlates with high luminescence efficiencies as expected from fundamental theory. This was indeed the case. There was, however, no clear trend with respect to the PbI_2 excess. The samples showed strong variations from measurement to measurement, possibly due to a reversible instability related to hysteresis and introduced by degradation as the devices have been stored for some time before the measurements. The highest value of the external electroluminescence quantum efficiency (EQE EL) in this series was measured for a -5 % device and approached 0.8 % at a current of 20 mA/cm^2. This is in good agreement with a V_{oc} of 1.2 V[5,19] and is as far as we know a record value. The EQE EL shown in figure 17.f increases approximately linearly with driving current as expected for a trap-recombination limited current[20]. The hysteresis in the EQE EL indicates that defect formation as a function of applied voltage influences the radiative recombination yield. In this case, the yield is larger when scanning from high bias back to 0 V and then also closer to the linear relation, whereas it is lower but superlinear when scanning forwards from 0 V. This is due to enhanced defect recombination, where the effect of the defects (their number, their cross section, their occupation) is reduced "in situ" during the sweep, thus resulting in the superlinear relation.

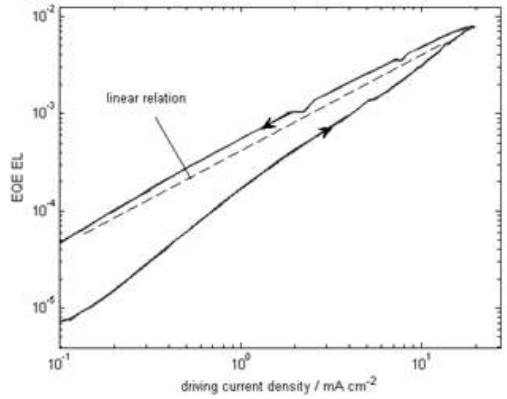

Figure S.12 EQE EL as a function of applied current for the -5% sample, scanned from 0 V to 1.5 V and back with a voltage sweep rate of 20 mV/s

Additional TEM images

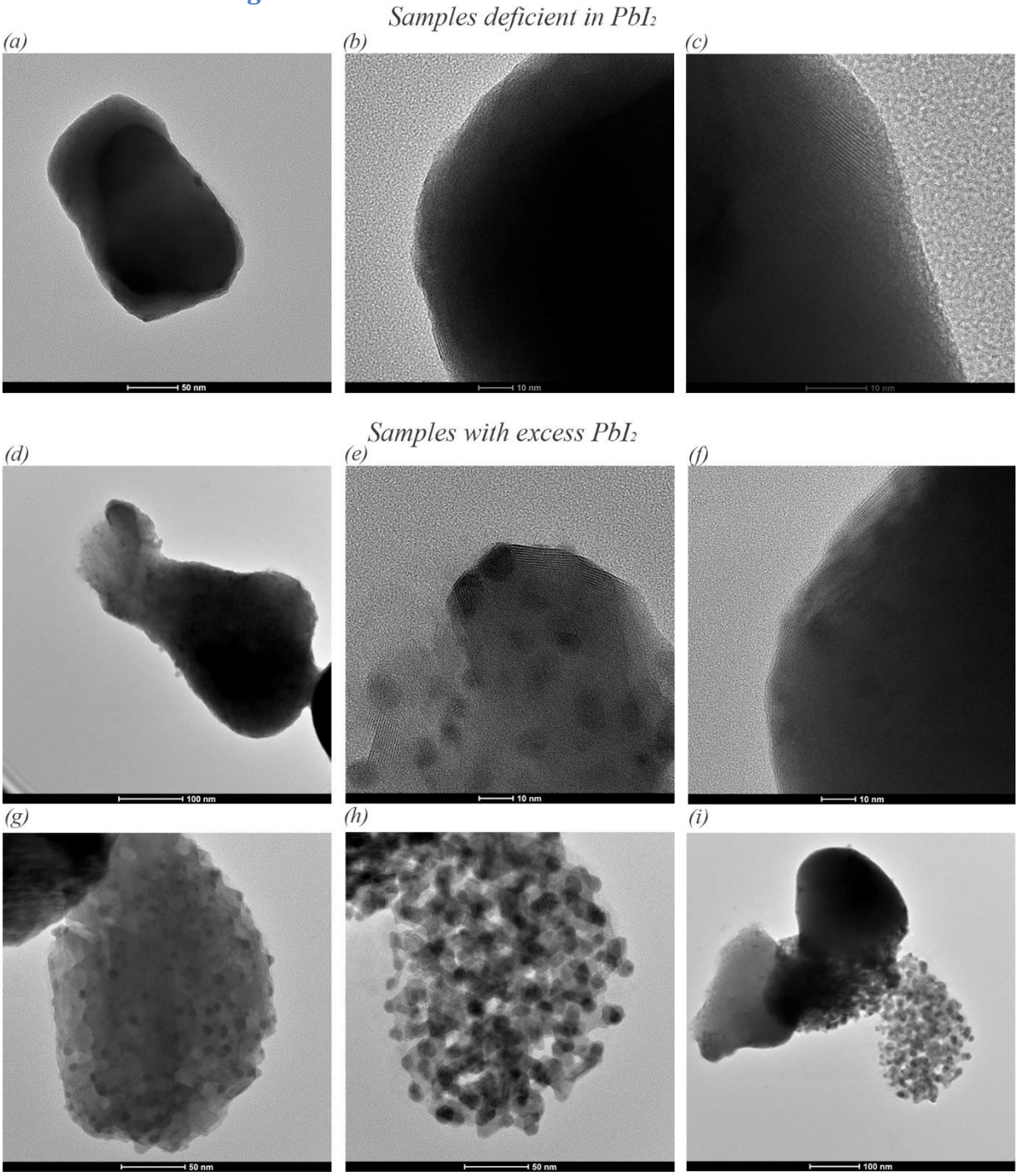

Figure S.13. (a)-(c). TEM images of a PbI_2-deficient sample. (d)-(i). TEM images of a PbI_2-rich sample. (g) and (h) is an image of the same spot illustrating sample degradation under the electron beam. (i) The same part as in (h) together with a previously unexposed grain. The samples were prepared by scratching of a perovskite film deposited on SLG with a razor blade, in which the TEM-grid then was rubbed.

Additional SEM images

Top view SEM images taken at six different magnifications are given in figure S.14-19. A larger version of the cross section images in the main article is given in figure S.20.

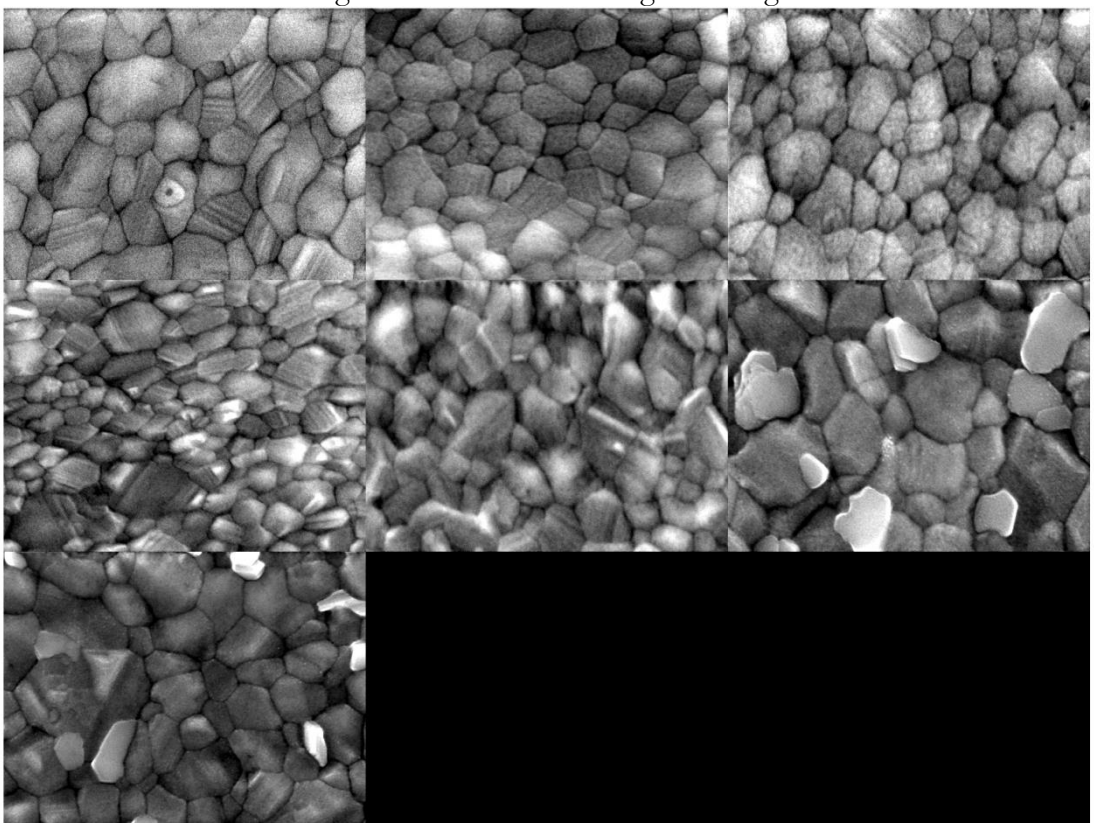

Figure S.14. SEM images of samples with seven different stoichiometries. Starting from the upper left corner and going from left to right the compositions are: -10 %, -5 %, 0 %, 5 %, 10 %, 15 %, 20% according the notation established in the experimental section. The width of each panel is 1.7 μm.

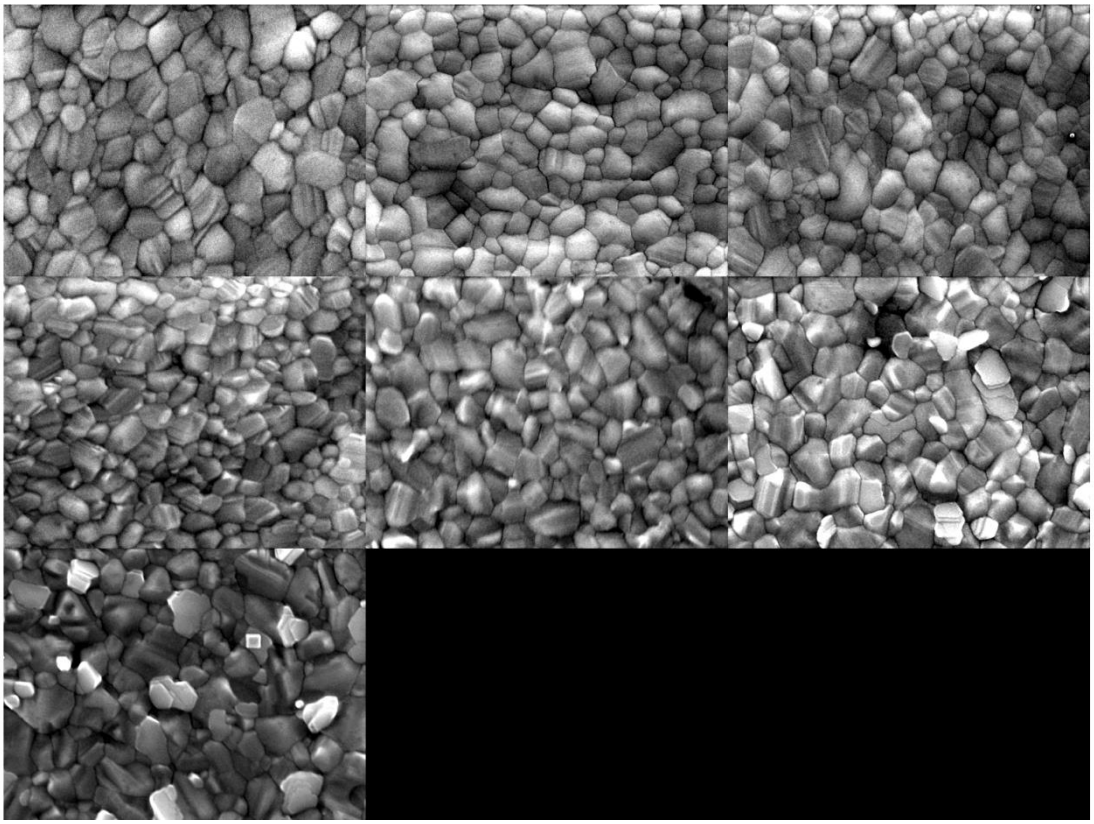

Figure S.15. The same samples as in figure S.7 but at a lower magnification. The width of each panel is 2.5 μm.

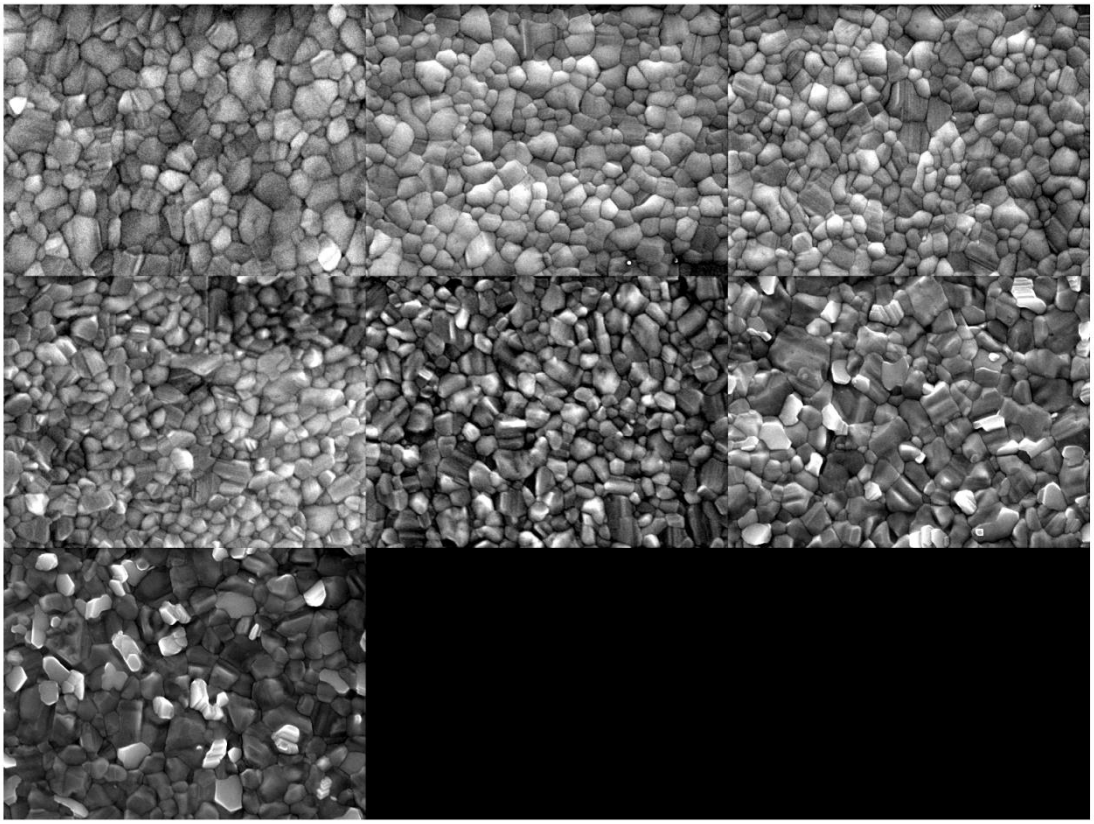

Figure S.16. The same samples as in figure S.7 but at a lower magnification. The width of each panel is 3.3 μm.

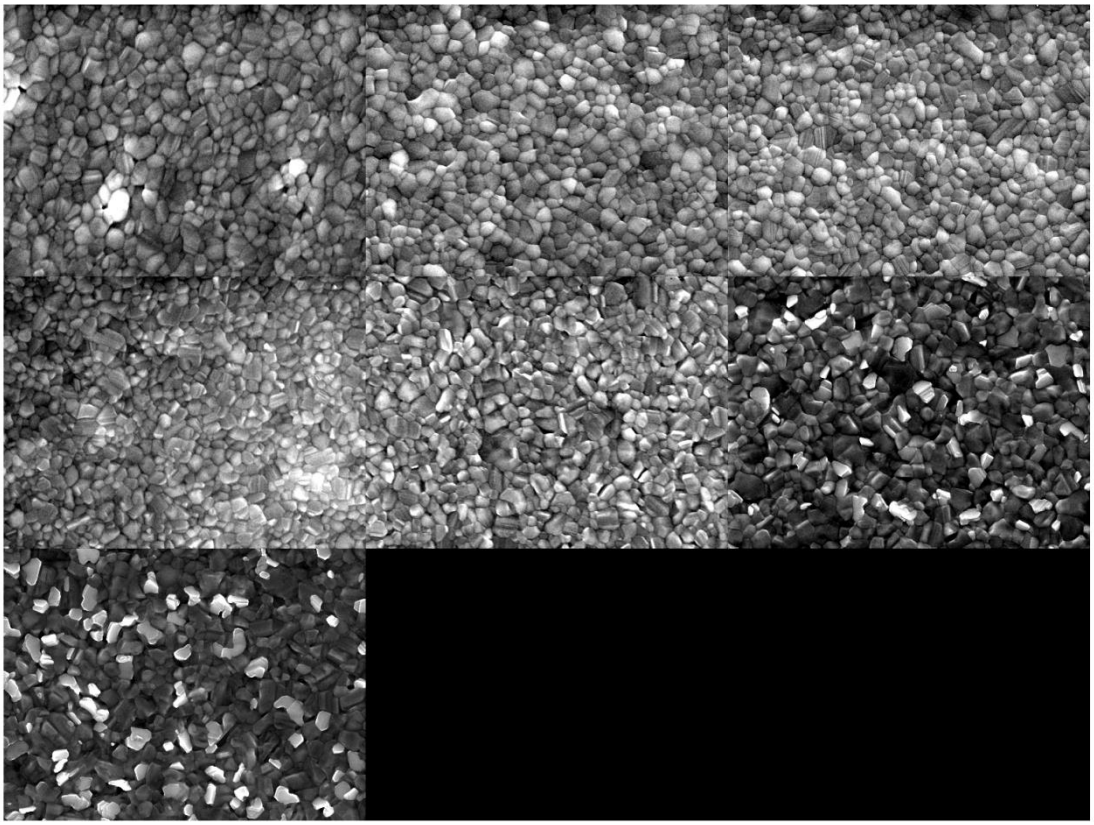

Figure S.17. The same samples as in figure S.7 but at a lower magnification. The width of each panel is 5.0 μm.

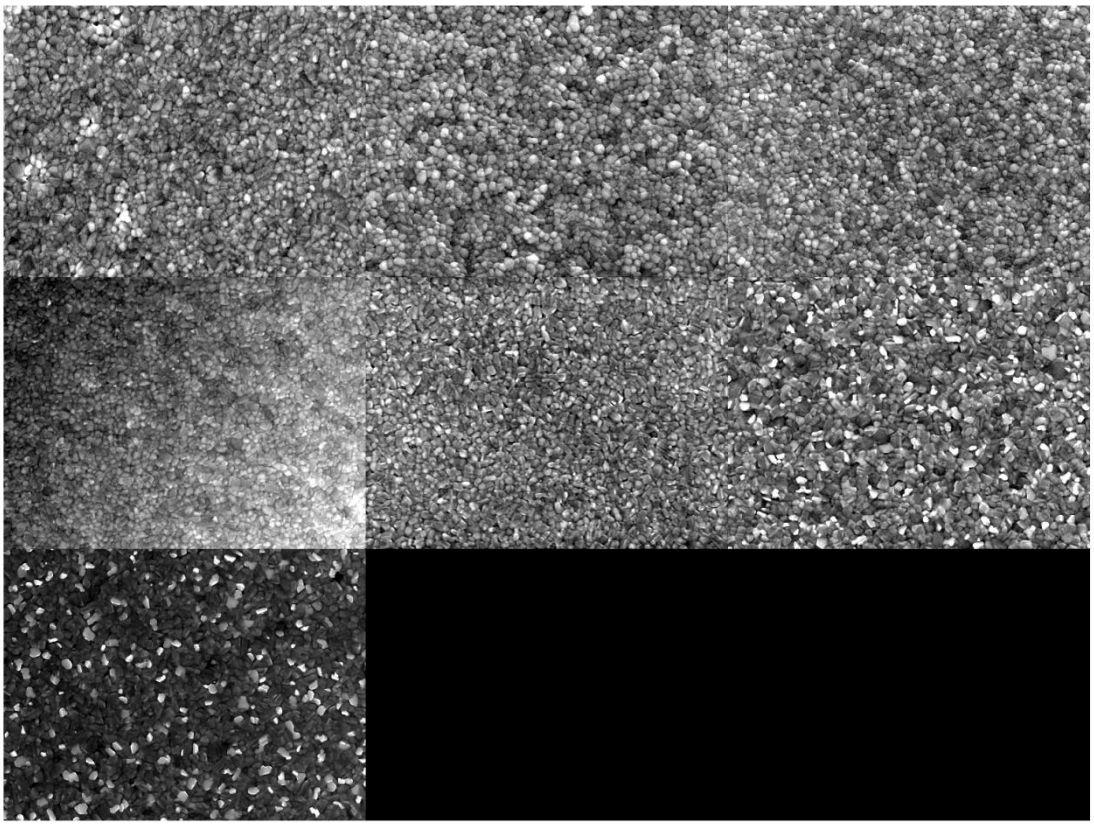

Figure S.18. The same samples as in figure S.7 but at a lower magnification. The width of each panel is 10 μm.

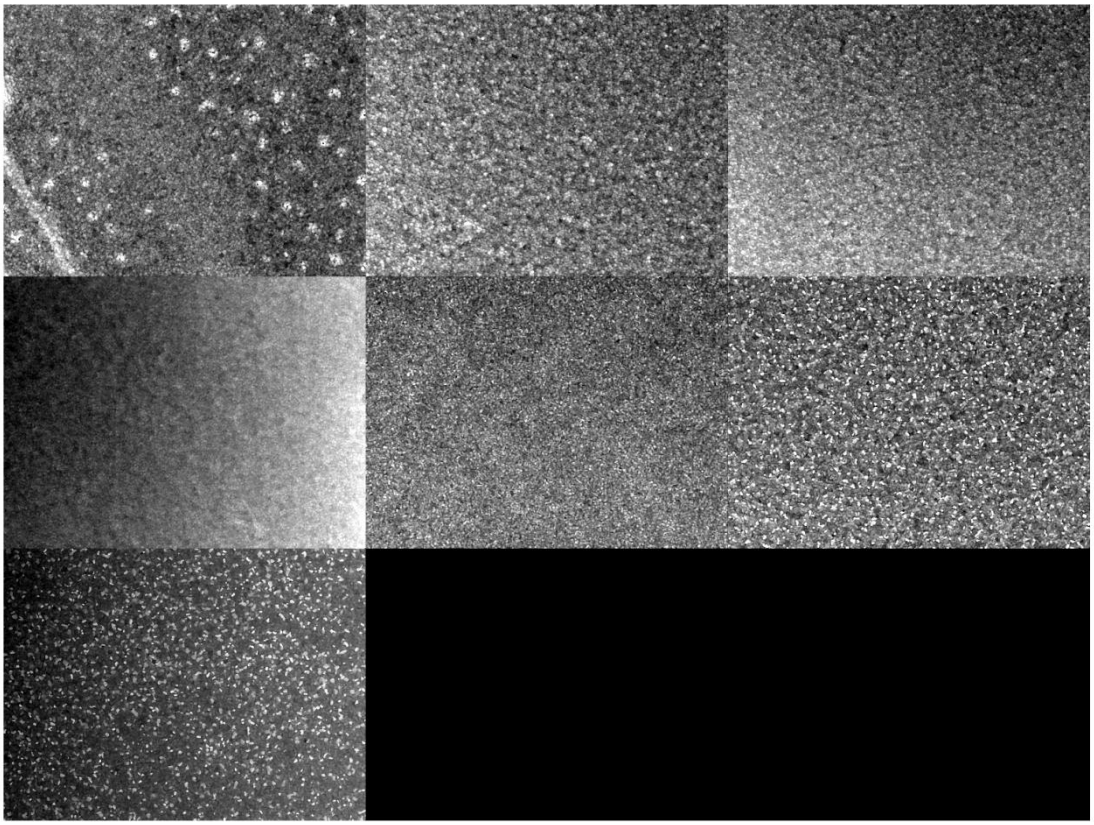

Figure S.19. The same samples as in figure S.7 but at a lower magnification. The width of each panel is 25 μm.

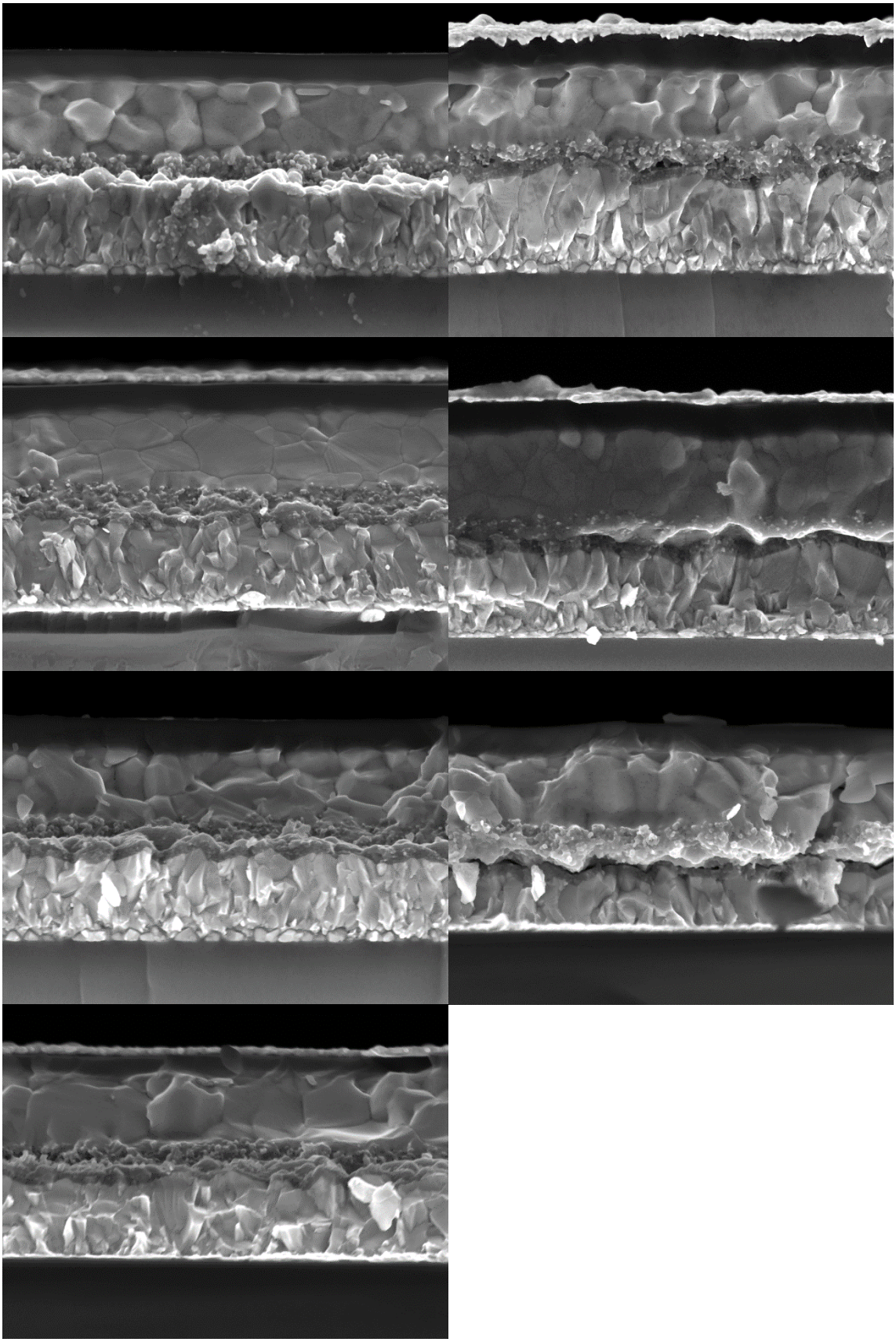

Figure S.20. A larger version of the cross section images found in the main article. Starting from the upper left corner and going from left to right the compositions are: -10 %, -5 %, 0 %, 5 %, 10 %, 15 %, 20%

References

(1) Baena, J. P. C.; Steier, L.; Tress, W.; Saliba, M.; Neutzner, S.; Matsui, T.; Giordano, F.; Jacobsson, T. J.; Kandada, A. R. S.; Zakeeruddin, S. M.; Petrozza, A.; Abate, A.; Nazeeruddin, M. K.; Graetzel, M.; Hagfeldt, A. *Energ. Environ. Sci.* **2015**, *8*, 2928.

(2) Giordano, F.; Abate, A.; Correa Baena, J. P.; Saliba, M.; Matsui, T.; Im, S. H.; Zakeeruddin, S. M.; Nazeeruddin, M. K.; Hagfeldt, A.; Graetzel, M. *Nat Commun* **2016**, *7*.

(3) Jesper Jacobsson, T.; Correa-Baena, J.-P.; Pazoki, M.; Saliba, M.; Schenk, K.; Gratzel, M.; Hagfeldt, A. *Energ. Environ. Sci.* **2016**, *9*, 1706.

(4) Roldan-Carmona, C.; Gratia, P.; Zimmermann, I.; Grancini, G.; Gao, P.; Graetzel, M.; Nazeeruddin, M. K. *Energ. Environ. Sci.* **2015**, *8*, 3550.

(5) Bi, D.; Tress, W.; Dar, M. I.; Gao, P.; Luo, J.; Renevier, C.; Schenk, K.; Abate, A.; Giordano, F.; Correa Baena, J.-P.; Decoppet, J.-D.; Zakeeruddin, S. M.; Nazeeruddin, M. K.; Grätzel, M.; Hagfeldt, A. *Sci. Adv.* **2016**, *2*.

(6) Zhao, Y.; Zhu, K. *J. Phys. Chem. Lett* **2014**, *5*, 4175.

(7) Xiao, M.; Huang, F.; Huang, W.; Dkhissi, Y.; Zhu, Y.; Etheridge, J.; Gray-Weale, A.; Bach, U.; Cheng, Y.-B.; Spiccia, L. *Angew. Chem. Int. Edit.* **2014**, *53*, 9898.

(8) Jeon, N. J.; Noh, J. H.; Kim, Y. C.; Yang, W. S.; Ryu, S.; Il Seol, S. *Nat. Mater.* **2014**, *13*, 897.

(9) Abate, A.; Leijtens, T.; Pathak, S.; Teuscher, J.; Avolio, R.; Errico, M. E.; Kirkpatrik, J.; Ball, J. M.; Docampo, P.; McPherson, I.; Snaith, H. J. *Phys. Chem. Chem. Phys.* **2013**, *15*, 2572.

(10) Abate, A.; Staff, D. R.; Hollman, D. J.; Snaith, H. J.; Walker, A. B. *Phys. Chem. Chem. Phys.* **2014**, *16*, 1132.

(11) Philippe, B.; Hahlin, M.; Edstrom, K.; Gustafsson, T.; Siegbahn, H.; Rensmo, H. *J. Electrochem. Soc.* **2016**, *163*, A178.

(12) Gorgoi, M.; Svensson, S.; Schaefers, F.; Ohrwall, G.; Mertin, M.; Bressler, P.; Karis, O.; Siegbahn, H.; Sandell, A.; Rensmo, H.; Doherty, W.; Jung, C.; Braun, W.; Eberhardt, W. *Nuclear Instruments & Methods in Physics Research Section a-Accelerators Spectrometers Detectors and Associated Equipment* **2009**, *601*, 48.

(13) Bassler, M.; Forsell, J. O.; Bjorneholm, O.; Feifel, R.; Jurvansuu, M.; Aksela, S.; Sundin, S.; Sorensen, S. L.; Nyholm, R.; Ausmees, A.; Svensson, S. *J. Electron. Spectrosc.* **1999**, *101*, 953.

(14) Scofield, J. H. *J. Electron. Spectrosc.* **1976**, *8*, 129.

(15) Yeh, J.; Lindau, I. *Atomic data and nuclear data tables* **1985**, *32*, 1.

(16) Jacobsson, T. J.; Schwan, L. J.; Ottosson, M.; Hagfeldt, A.; Edvinsson, T. *Inorg. Chem.* **2015**, *54*, 10678.

(17) Jacobsson, T. J.; Pazoki, M.; Hagfeldt, A.; Edvinsson, T. *J. Phys. Chem. C* **2015**, *119*, 25673.

(18) Correa-Baena, J.-P.; Anaya, M.; Lozano, G.; Tress, W.; Domanski, K.; Saliba, M.; Matsui, T.; Jacobsson, T. J.; Calvo, M. E.; Abate, A.; Grätzel, M.; Míguez, H.; Hagfeldt, A. *Adv. Mater.* **2016**, *28*, 5031.

(19) Tress, W.; Marinova, N.; Inganas, O.; Nazeeruddin, M. K.; Zakeeruddin, S. M.; Graetzel, M. *Adv. Energ. Mater.* **2015**, *5*.

(20) Marinova, N.; Tress, W.; Humphry-Baker, R.; Dar, M. I.; Bojinov, V.; Zakeeruddin, S. M.; Nazeeruddin, M. K.; Gratzel, M. *Acs Nano* **2015**, *9*, 4200.